iScience

CellPress
OPEN ACCESS

Article

Active disturbance rejection control of drag-free satellites considering the effect of micro-propulsion noise

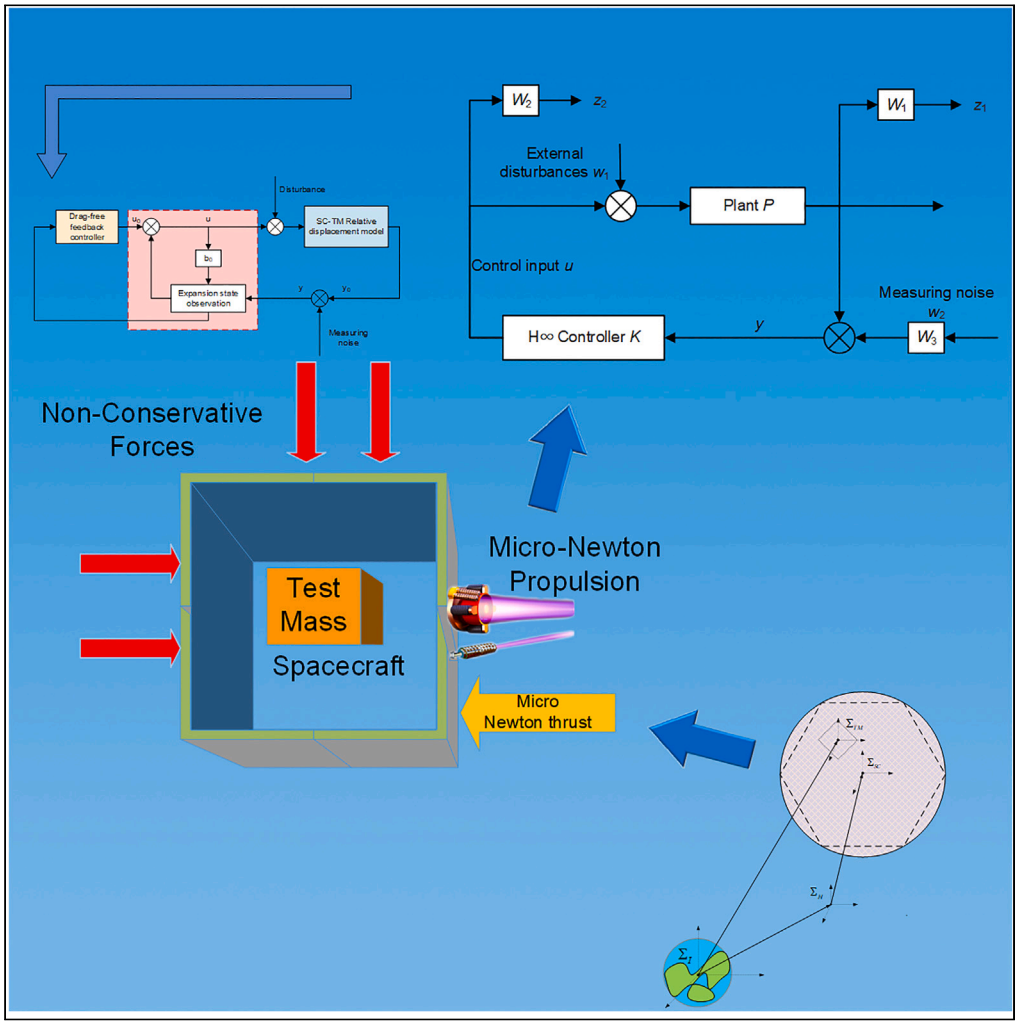

Junjie Zhou,
Aiping Pang,
Hongbo Zhou

appang@gzu.edu.cn

Highlights

The H_∞ controller is designed as an active disturbance rejection feedback controller

The disturbance is estimated and feedforward compensated by an extended state observer

Achieve the relative displacement of 2 nm/Hznm/$Hz^{1/2}$ for the drag-free satellite platform

Achieve the residual acceleration of 1×10^{-15} m/sm/s^2/$Hz^{1/2}$ for the test mass

Zhou et al., iScience 26, 107213
July 21, 2023
https://doi.org/10.1016/j.isci.2023.107213

iScience

CellPress
OPEN ACCESS

Article

Active disturbance rejection control of drag-free satellites considering the effect of micro-propulsion noise

Junjie Zhou,[1] Aiping Pang,[1,2,*] and Hongbo Zhou[1]

SUMMARY

The space gravitational wave detection mission requires a super "static and precise" scientific experiment environment. In order to solve the non-conservative force disturbance variation and the actuator noise and measurement noise, this paper designs a drag-free control scheme based on active disturbance rejection control (ADRC) framework to achieve the high-precision index. According to the ultra-high accuracy, low bandwidth limitation, and robustness requirements of drag-free satellite, the H_∞ controller satisfying the robustness constraint is designed as an active disturbance rejection feedback controller to achieve the high-precision index. Meanwhile, the non-conservative force disturbance with a wide range of variations is estimated and feedforward compensated by an extended state observer to improve the system robustness. Simulation results show that the control system can achieve the relative displacement of 2 nm/Hznm/$Hz^{1/2}$ for the drag-free satellite platform and the residual acceleration of 1×10^{-15} m/sm/s^2/$Hz^{1/2}$ for the test mass.

INTRODUCTION

The existence of gravitational waves was theoretically predicted by Einstein's theory of general relativity in 1915, and since then many scholars have tried to prove the existence of gravitational waves by directly detecting their signals. In 2015, the Laser Interferometric Gravitational Wave Observatory (LIGO) in the United States successfully made the first direct observation of gravitational waves. For the detection of gravitational waves using laser interferometers, the closer the arm length is to the wavelength of the gravitational waves, the higher the detection sensitivity will be. However, the limited arm length of ground-based laser interferometers, as well as the effects of ground vibrations and changes in the gravitational gradient of the earth's surface, produces significant low-frequency noise, making it difficult for ground-based interferometers to detect gravitational wave signals in the low-frequency band. In the space environment, the laser interferometric arms created by satellite formation can reach hundreds of thousands to millions of kilometers in length, while avoiding the effects of surface vibrations, allowing the detection of gravitational wave signals in the millihertz band.[1]

Precision measurement missions in space often rely on a critically low disturbance environment, where the residual disturbance acceleration of the mission platform on board the satellite is required to be as low as possible. Drag-free control takes the suspended TM placed inside the spacecraft in a vacuum cavity as the reference frame, and generates a thrust of equal magnitude and opposite direction to the external disturbance through the thrusters to counteract the non-conservative force interference, so that the satellite platform and the TM can move synchronously, which is called the "drag-free" state. Drag-free control is designed to achieve the stringent operational objectives (ultra-low noise, ultra-high accuracy, and ultra-high stability) of the scientific experiment platform inside the satellite, and its principal schematic is shown in Figure 1. The concept of drag-free control first appeared in the 1960s and was systematically investigated by B. Lange in his PhD thesis which was successfully applied to the first drag-free satellite launched by the US Navy (Triad I experimental satellite) for validation.[2] Depending on the requirements and characteristics of the application, drag-free control can be divided into two modes: displacement mode and accelerometer mode.[3,4] The displacement mode uses displacement measurement techniques such as capacitive displacement sensors to measure the relative displacement between the satellite and the TM, and controls the thrust based on the resulting displacement error to make the satellite follow the TM. In the

[1]College of Electrical Engineering, Guizhou University, Guiyang 550025, China

[2]Lead contact

*Correspondence: appang@gzu.edu.cn

https://doi.org/10.1016/j.isci.2023.107213

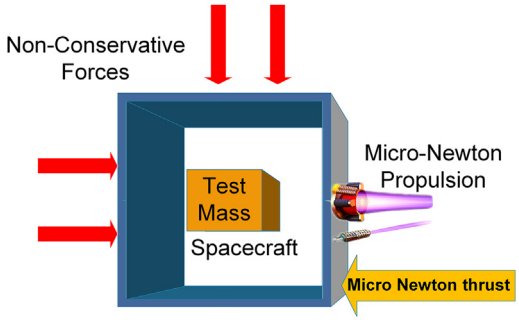

Figure 1. Schematic diagram of drag-free control

accelerometer mode, the TM and the cavity in which it is located are combined to act as an accelerometer (inertial sensor). The TM is controlled by electrostatic forces to follow the motion of the satellite to measure the disturbing acceleration of the satellite so as to regulate the thrust of the thrusters.

Up to now a number of satellites with different applications have adopted drag-free control and have been validated in orbit. The TRIAD I drag-free satellite (1972) was applied for navigation and positioning, and the classical on-off control method was used to design the controller due to the limitations of the propulsion system. Residual acceleration of its TM was achieved with an accuracy of 10^{-10} m/sm/s^2/Hz$^{1/2}$. As the control parameters were constantly switched between on-off, the drag-free control system was prone to oscillations leading to a decrease in residual acceleration.[5] The GP-B satellite (2004), applied to fundamental physics, achieved a TM residual acceleration of 10^{-12} m/sm/s^2/Hz$^{1/2}$ using classical proprotion integration differentiation (PID) control.[6] The gravity measurement satellite GOCE (2009) used the Embedded Model Control Method (EMC) to design the controller, achieving accuracy of 10^{-8} m/sm/s^2/Hz$^{1/2}$ for the satellite's residual acceleration and 3×10^{-12} m/sm/s^2/Hz$^{1/2}$ for the TM residual acceleration.[7–9]

Gravitational wave detection places unprecedented accuracy requirements on satellite platforms, and European Space Agency (ESA)'s laser interferometer space antenna (LISA) project first proposed a drag-free target of up to 10^{-15} m/sm/s^2/Hz$^{1/2}$, which was verified in orbit by using the H_∞ loop forming technique[10] for controller design on its Pathfinder experimental satellite launch, where the TM residual acceleration achieved a residual acceleration of 10^{-15} m/sm/s^2/Hz$^{1/2}$.[11–13] China carried out its gravitational wave detection mission in 2015 and launched the Tianqin-1 and Taiji-1 experimental satellites in 2019, with the residual acceleration of the Tianqin-1 satellite reaching 3×10^{-9} m/sm/s^2/Hz$^{1/2}$[14] and the Taiji-1 satellite reaching 10^{-8} m/sm/s^2/Hz$^{1/2}$.[15] LISA Pathfinder uses a displacement mode, while the drag-free control adopted by Taiji-1 and Tianqin-1 are both accelerometer modes. The discrepancy between the residual acceleration and the accuracy required for gravitational wave detection is four orders of magnitude, and there is still a significant gap in China's drag-free control technology for gravitational wave detection, which needs further exploration and research.

The gravitational wave scientific detection band is 0.1mHz–1Hz, and in order to ensure the measurement accuracy of gravitational wave detection, high microgravity level requirements are imposed on the satellite platform, and a 10^{-15} m/Hzm/Hz$^{1/2}$ residual acceleration constraint is imposed on the inspection mass in the 0.1mHz–1Hz band, and the inspection mass is affected by the rigid coupling force, and this force is influenced by the relative displacement of the satellite and the inspection constraint, so a 4 nm/Hznm/Hz$^{1/2}$ requirement is imposed on the relative displacement in the gravitational wave detection band. The ultra-low frequency band of the detection target and ultra-high accuracy requirements, but there are many problems such as model uncertainty, non-linearity, inherent low-frequency interference, output safety boundaries of the micro-propulsion system, and external interference from the complex space environment. These problems bring great challenges to the realization of the drag-free index, and the current drag-free control accuracy is still far from meeting the index requirements of gravitational wave detection. The feedback control framework cannot balance the bandwidth limitation and accuracy requirements, and in the 1990s, Mr. Jingqing Han, a famous control expert in China, proposed active disturbance rejection control (ADRC). The method summaries all uncertainties acting on the controlled object (including model uptake, internal and external disturbances, and non-linearities) as "total disturbance" other than the integral standard type, and uses an extended state observer (ESO) to estimate and feedforward compensate

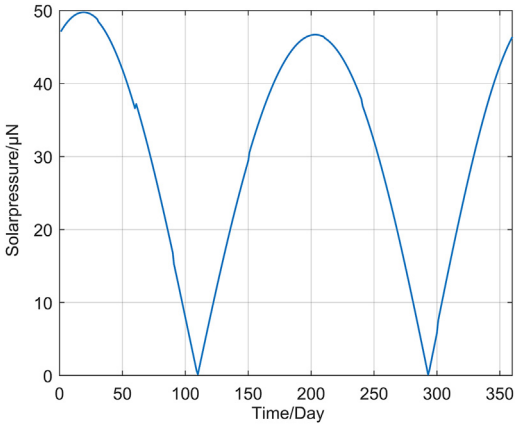

Figure 2. Solar pressure range

for the disturbances before they cause errors in the system. A large number of theoretical[16–21] and applied[22–26] studies have shown that ADRC is effective in controlling systems with unmodelled dynamics, parameter perturbation, and external disturbances, with high robustness and immunity to disturbances. In recent years, the influence of ADRC has been increasing, and its theoretical research has flourished and has been widely and effectively applied in engineering. Due to the non-linear and non-smooth feedback structure used in the original ADRC, its theoretical analysis is very difficult and many controller parameters need to be adjusted. In order to simplify the analysis and implementation of ADRC, the literature[27–29] investigated the linear ADRC method for different types of uncertain systems and focused on the convergence of Linear Active Disturbance Rejection Control (LADRC), revealing the quantitative relationship between system performance and control parameters.

In this paper, in response to the complex non-conservative force interference, the high accuracy control requirement of 4 nm/Hznm/$Hz^{1/2}$ and the 0.1Hz bandwidth limitation problem faced by the drag-free control system in the gravitational wave detection mission, we adopt the self-*anti*-disturbance control method, which uses the ESO to observe and compensate the disturbance, and the H_∞ feedback control method in the controller part to obtain a drag-free control design scheme suitable for the gravitational wave detection mission. The relative displacements of the satellite and test masses for drag-free control are modeled, and the system characteristics and performance requirements are analyzed. A linear ESO is first designed to estimate perturbations and perform feedforward compensation for non-conservative force disturbances that cannot be accurately modeled in complex spatial environments. Then, for the high accuracy requirements of the system, bandwidth limitations and the uncertainty effects of the unmodeled dynamics of the system, an H_∞ feedback controller is designed and embedded into the ADRC framework, and a detailed analysis of the system performance and controller performance after control is presented in detail. The disturbance and noise signals used in the simulation are given, and the effectiveness of the control system is verified by simulating and analyzing the drag-free control system with the ADRC designed in this paper.

RESULTS AND DISCUSSION

Performance analysis of drag-free control system

In the gravitational wave detection mission in space, the orbit altitude of the gravitational wave detection satellite is generally in the order of 100,000 km, so the main non-conservative force in the space environment is not the atmospheric disturbance but the solar pressure, we take the non-towing satellite in the "Tianqin project" as an example, according to the calculation in the literature, we can get the solar pressure range of 0–50μN during the operation of the Tianqin satellite. According to the calculations in the literature, we can obtain the solar pressure during the operation of the Tianqin satellite in the range of 0–50μN, as shown in Figure 2.

We also consider the effects of solar pressure noise, actuator noise, and measurement noise on the drag-free control system to verify the effectiveness of the controller designed based on the self-turbulence control scheme. In this paper, we set the solar pressure noise as 0.1uN/$Hz^{1/2}$, the actuator noise

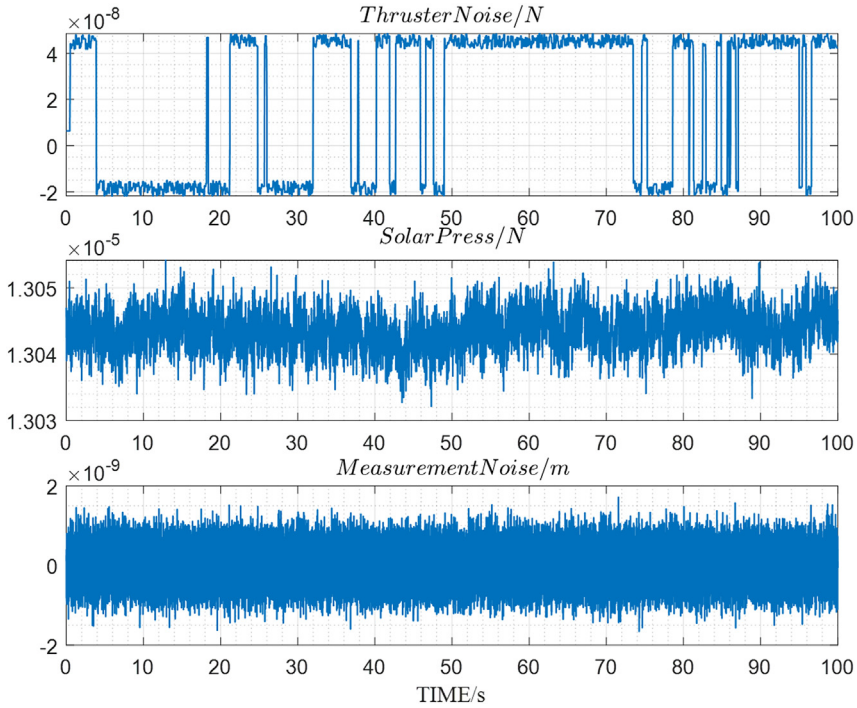

Figure 3. Time domain signal plot of each noise

as 0.1–1uN/Hz$^{1/2}$, and the measurement noise as 1.7 nm/Hznm/Hz$^{1/2}$, and the time domain simulation signal of solar pressure in 1000s is shown in Figure 3.

Since the simulation duration cannot completely cover the variation range of solar pressure, we selected two characteristic points representing solar pressure as 11μN, in the simulation process, 44μN and simulated the robust integrated control scheme containing only H_∞ controller and the self-anti-disturbance control based on the design of this paper, respectively, to verify the effectiveness of the designed control scheme.

(1) Feedback controller effect analysis

Figure 4 shows the simulation results of drag-free control with H_∞ control method for different solar pressure perturbations. Under the small light pressure (≈11μN) perturbation, the H_∞ controller can guarantee the relative displacement error between 2 nm/Hznm/Hz$^{1/2}$@0.02Hz. But the drag-free control effect decreases significantly with the increase of solar pressure perturbation (≈44μN), the relative displacement error noise spectrum is 20 nm/Hznm/Hz$^{1/2}$@0.02Hz, increasing by one order of magnitude overall. It can be seen that due to the strong robustness of the H_∞ controller, the designed controller cannot be guaranteed to meet the drag-free control accuracy requirements in the process of a wide range of external disturbances.

(2) Disturbance observation analysis

According to the observation design for external disturbances, Figure below Equation 11 shows that the observation bandwidth of the dilated state observer directly determines the observation effect for the disturbance, while the response speed of the observer increases with the increase of the observation bandwidth. The observer BODE plots for different observing bandwidth designs are shown in Figure 5.

The magnitude characteristics of the observer do not exceed the 0dB line when the observing bandwidth is 1 rad/s. As the setting value of the observing bandwidth is increased (2.5, 5, and 10 rad/s), the magnitude

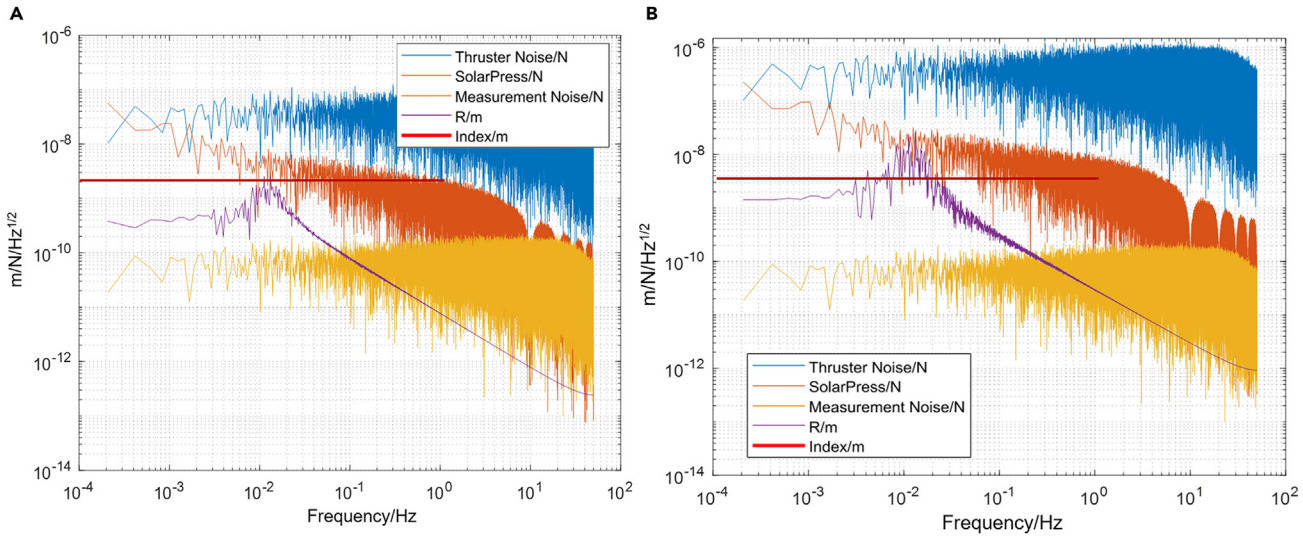

Figure 4. Amplitude spectral density (ASD) of relative displacement and each noise signal based on H_∞ control

(A)Solar pressure of 11μN.

(B)Solar pressure of 44μN.

characteristics of the observer cross the 0 dB line and the greater the observer shear frequency. For the gravitational wave detection mission, the controller bandwidth needs to be controlled within 0.1 Hz, and the amplitude and frequency characteristics of the observer larger than 0dB have an amplifying effect on the noise, and cannot be suppressed by the controller. By analyzing the observation and compensation effects of external disturbances at different bandwidths, as shown in Figure 6, the impact of the measurement noise on the disturbance observations is more significant as the bandwidth increases, and then there is a significant high-frequency variation in the control input when the corresponding compensation force is generated according to the disturbance observations. When the observation bandwidth is set to 10 rad/s, the corresponding control force changes across 20μN in 0.1s, which is obviously beyond the output constraint of the micro-nuclidean thruster, so the observer bandwidth needs to be limited to a certain extent, and the final observation bandwidth selected in this paper is 2.5 rad/s.

Figure 7 shows the simulation results of the noise spectrum density of the satellite platform designed by the self-turbulence control method for different solar light pressure perturbations. The relative

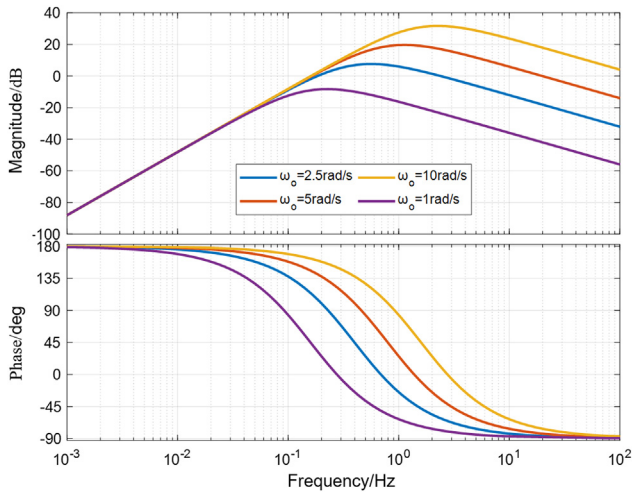

Figure 5. BODE plots of the observer with different observation bandwidth designs

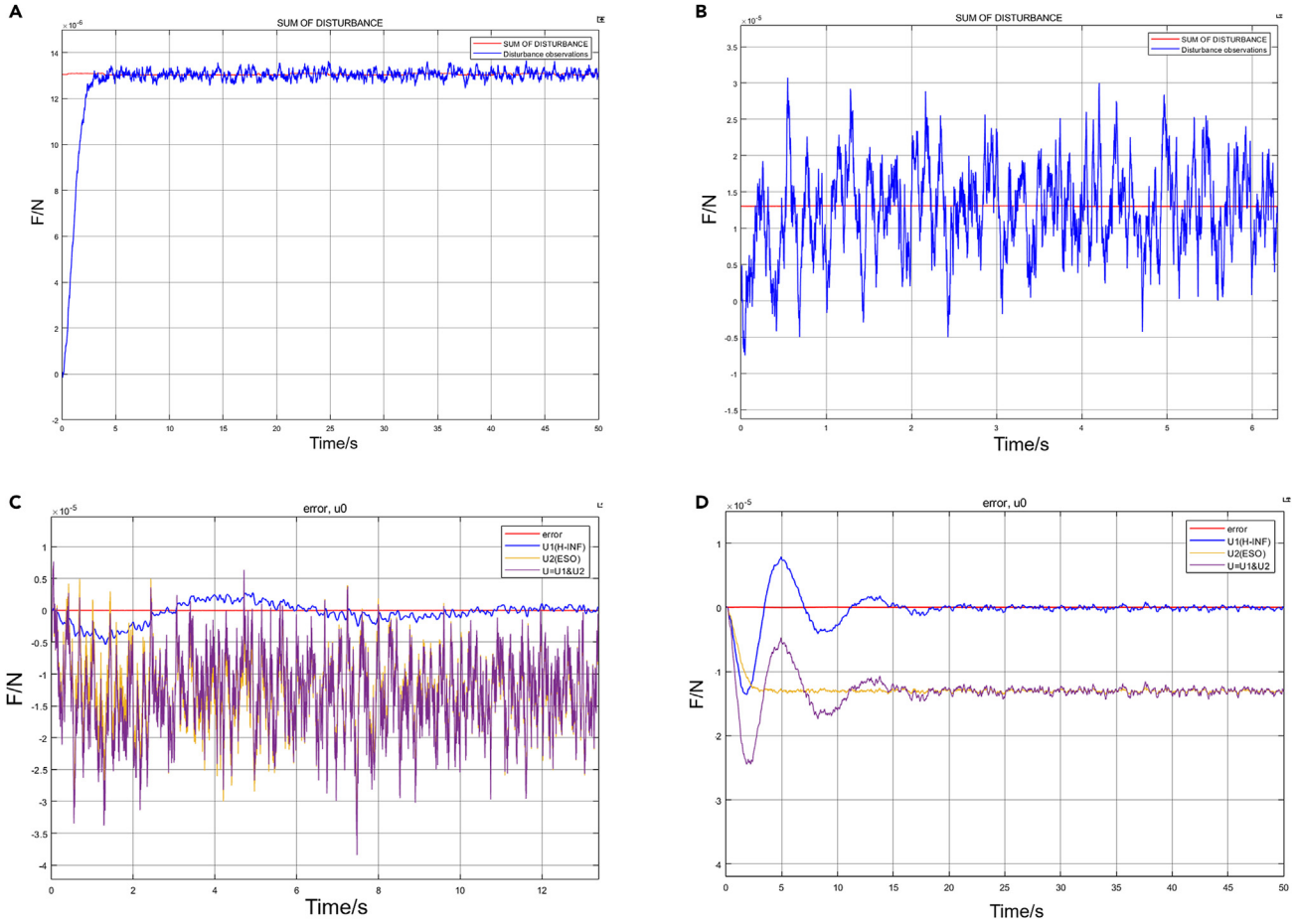

Figure 6. The effect of disturbance observation and control input force effect under different observation bandwidth: the upper figure shows the comparison of disturbance observation value; the lower figure shows the comparison of control force output

(A) The comparison of disturbance observation value under 5 rad/s observation bandwidth.

(B) The comparison of disturbance observation value under 10 rad/s observation bandwidth.

(C) The comparison of control force output under 5 rad/s observation bandwidth.

(D) The comparison of control force output under 10 rad/s observation bandwidth.

displacement error noise spectrum of the drag-free satellite achieves the control accuracy of 2 nm/Hznm/$Hz^{1/2}$@1mHz–1Hz for both small ≈11μN (Figure 7A) and large ≈44μN (Figure 7B) light pressure perturbations, without any degradation of the control accuracy due to large changes in external light pressure perturbations.

Figure 8 shows the simulation results of the control input U for a large optical pressure disturbance (≈44μN) with H_∞ control and self-rejecting control methods: the U(ADRC) consists of the self-rejecting feedback controller input U1 and the disturbance compensation input U2 generated by the dilated state observer; the H_∞ control input is U(H-INF). The results show that a drag-free control scheme based on the self-rejecting control design, with feedforward compensation to the H_∞ feedback controller through the perturbation compensation generated by the state observer, can significantly reduce the pressure on the H_∞ feedback controller, while speeding up the system response to a certain extent.

The results in Figure 9 show the time domain simulation signals of the relative displacement error of the satellite and the TM and the residual acceleration of the TM for two different control schemes, showing that the relative displacement of both is less than 0.1μm in the time domain simulation, which satisfies the time domain performance index of the system, but the relative error of the self-turbulence control is twice as low as that of the simple H_∞ controller and has a faster response.

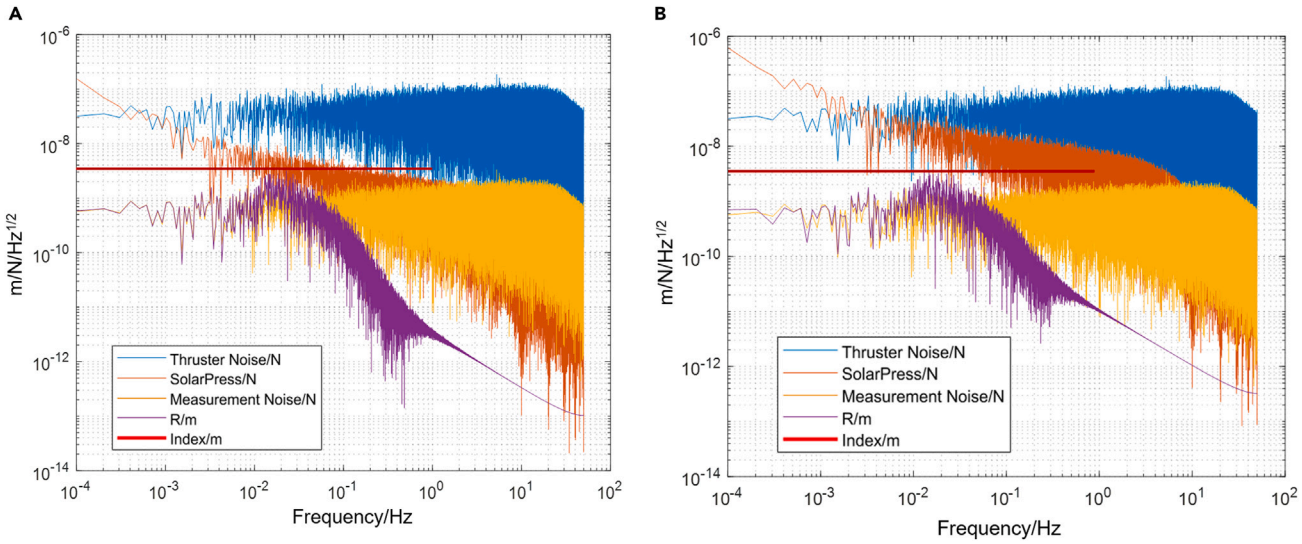

Figure 7. Relative displacement and amplitude spectral density (ASD) of each noise signal under self-turbulence drag-free control

(A) Solar pressure of 10μN magnitude.

(B) Solar pressure of 44μN magnitude.

Conclusions

The space gravitational wave detection mission puts forward difficult requirements for the control of drag-free satellites. To address the problem of incompatibility between the high accuracy and stability requirements, the ultra-low bandwidth and robustness requirements of the drag-free control system for gravitational wave detection, this paper designs controllers to meet the requirements of high accuracy and strong robustness of the system based on an ADRC framework. The complex disturbances to which the system is subjected are estimated by an ESO followed by feedforward compensation, and the feedback control is based on H_∞ control theory to design a high-precision optimized controller that satisfies robustness constraints, both of which form a self-anti-disturbance control framework. The simulation results show that the

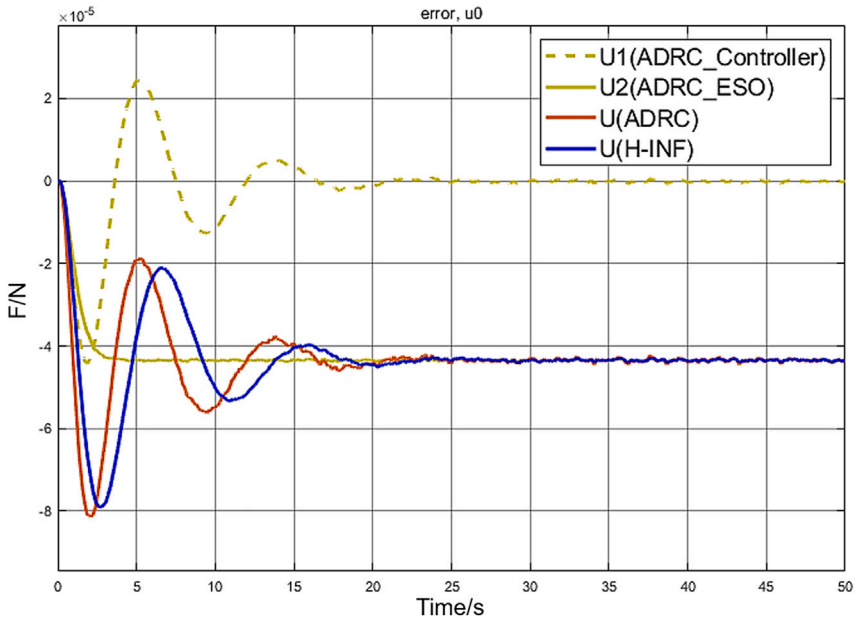

Figure 8. Comparison of control input U under H_∞ control and self-anti-disturbance control

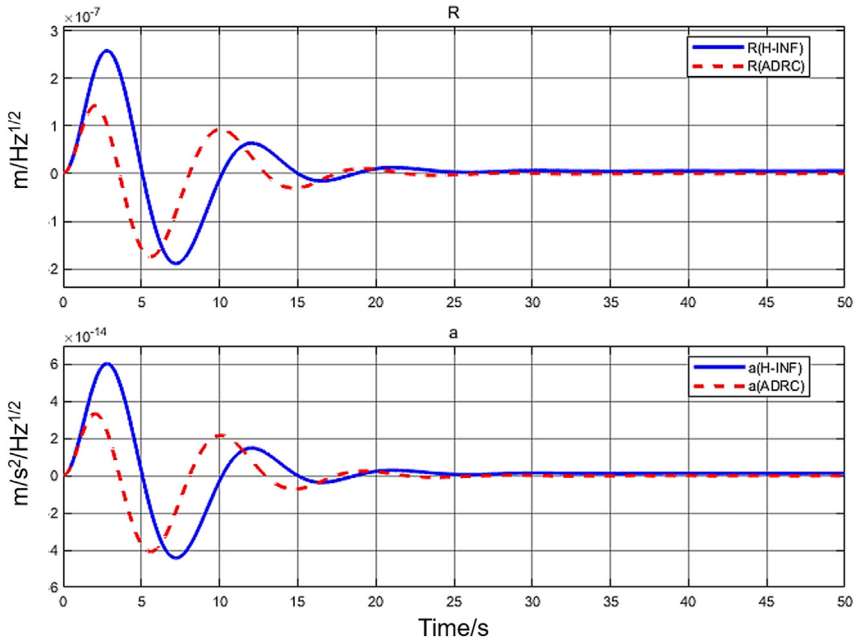

Figure 9. Time domain simulation results under H_∞ control and self-anti-disturbance control

designed state observer can estimate the external disturbance of the system faster and more accurately, as well as compensate the feedforward in time. The designed H_∞ feedback controller can meet the system performance requirements, limit the system bandwidth to 0.1Hz, the relative displacement noise spectrum between the satellite and the detection mass reaches 2 nm/Hznm/$Hz^{1/2}$@1mHz–1Hz, which shows that the relative displacement in the gravitational wave sensitive frequency band (1mHZ–1Hz) meets the requirements of gravitational wave detection.

Limitations of the study

This paper adopts the previous drag-free satellite layout, but the future TM layout in spaceborne gravitational wave observatories as follows: a pair of TM are mounted on each of the three spacecraft forming the observatory, in order to build up two unaligned interferometer arms (actually three to close the triangle), to reveal the waves. Thus, each TM can only have a 1.5 drag-free direction (along the sensitive axis fixed by the interferometer arm and the common vertical to the arm plane). In order to address drag-free control to spaceborne gravitational wave observatories, we will account for this layout in the future.

STAR★METHODS

Detailed methods are provided in the online version of this paper and include the following:

- KEY RESOURCES TABLE
- RESOURCE AVAILABILITY
  - Lead contact
  - Material availability
  - Data and code availability
- EXPERIMENTAL MODEL AND SUBJECT DETAILS
  - Drag-free satellite motion modeling
  - System performance analysis and requirements
- METHOD DETAILS
  - Control system design based on ADRC
- QUANTIFICATION AND STATISTICAL ANALYSIS

ACKNOWLEDGMENTS

This work was supported by the National Natural Science Foundation of China (NNSF) of China under grant No.12162007, National Key R&D Program of China Key Project of Gravitational Wave Detection in 2020 (No.2020YFC2201000), and the Research on New Power System and Its Digital Engineering (QianJiaoJi, China [2022] 043).

AUTHOR CONTRIBUTIONS

Conceptualization, J.Z., H.Z., and A.P.; data curation, J.Z. and H.Z.; funding acquisition, A.P.; investigation, H.Z. and J.Z.; methodology, J.Z., A.P., and H.Z.; resources, A.P.; validation, J.Z. and H.Z.; visualization, H.Z.; writing—original draft, J.Z. and H.Z.; writing—review and editing, A.P. All authors have read and agreed to the published version of the manuscript.

DECLARATION OF INTERESTS

The authors declare no competing interests.

Received: November 7, 2022
Revised: March 13, 2023
Accepted: June 22, 2023
Published: June 28, 2023

REFERENCES

1. Wu, S.F., Wang, N., and Gong, D.R. (2020). Key technologies for scientific missions of gravitational wave detection. Journal of Deep Space Exploration *7*, 118–127. https://doi.org/10.15982/j.issn.2095-7777.2020.20190402001.

2. Lange, B. (1964). The drag-free satellite. AIAA J. *2*, 1590–1606. https://doi.org/10.2514/3.55086.

3. GIULICCHI, L., WU, S.F., and FENAL, T. (2013). Attitude and orbit control systems for the LISA pathfinder mission. Aero. Sci. Technol. *24*, 283–294. https://doi.org/10.1016/J.AST.2011.12.002.

4. Eleonora, C. (2020). LISA Pathfinder Noise Performance Results: Disturbances in the Sub-mHz Frequency Band and Projection to LISA (University of Trento). https://doi.org/10.15168/11572_254388.

5. Snyder, N.J., Williams, W.M., and Denton, D.L. (1974). A Satellite Freed of all but Gravitational Forces: "TRIAD I". J. Spacecraft Rockets *11*, 637–644. https://doi.org/10.2514/3.62146.

6. CHEN, J.H. (1984). Helium Thrustor Propulsion System for Precise Attitude Control and Drag Compensation of the Gravity Probe-B Satellite (Stanford University).

7. Evers, W.J. (2004). GOCE Dynamical Analysis and Drag Free Mode Control (Eindhoven University of Technology). Report No.: 2004.44. https://doi.org/10.1007/s00340-009-3776-5.

8. Prieto, D., and Ahmad, Z. (2005). A drag free control based on model predictive techniques. In Proceedings of the 2005, American Control Conference. 2005, pp. 1527–1532. https://doi.org/10.1109/ACC.2005.1470184.

9. Canuto, E. (2008). Drag-free and attitude control for the GOCE satellite. Automatica *44*, 1766–1780. https://doi.org/10.1016/j.automatica.2007.11.023.

10. Fichter, W., Gath, P., Vitale, S., and Bortoluzzi, D. (2005). LISA Pathfinder drag-free control and system implications. Classical Quant. Grav. *22*, 139–148. https://doi.org/10.1088/0264-9381/22/10/002.

11. Anderson, G., Anderson, J., Anderson, M., Aveni, G., Bame, D., Barela, P., Blackman, K., Carmain, A., Chen, L., Cherng, M., et al. (2018). Experimental results from the ST7 mission on LISA Pathfinder. Phys. Rev. D *98*, 102005. https://doi.org/10.1103/PhysRevD.98.102005.

12. Armano, M., Audley, H., Baird, J., Binetruy, P., Born, M., Bortoluzzi, D., Castelli, E., Cavalleri, A., Cesarini, A., Cruise, A., et al. (2019). LISA Pathfinder micronewton cold gas thrusters: In-flight characterization. Phys. Rev. D *99*, 122003. https://doi.org/10.1103/PhysRevD.99.122003.

13. Marie, J., Cordero, F., Milligan, D., Milligan, E., and Tatry, P. (2019). In-Orbit Experience of the Gaia and LISA Pathfinder Cold Gas Micro-propulsion Systems. In Space Operations: Inspiring Humankind's Future, H. Pasquier, C. Cruzen, M. Schmidhuber, and Y. Lee, eds. (Springer), pp. 551–574. https://doi.org/10.1007/978-3-030-11536-4_21.

14. Luo, J., Bai, Y.Z., Cai, L., Cao, B., Chen, W.M., Chen, Y., Cheng, D.C., Ding, Y.W., Duan, H.Z., Gou, X., et al. (2020). The first-round result from the TianQin-1 satellite. Classical Quant. Grav. *37*, 185013. https://doi.org/10.1088/1361-6382/aba66a.

15. Hu, Z., Wang, P., Deng, J., Cai, Z., Wang, Z., Wang, Z., Yu, J., Wu, Y., Kang, Q., Li, H., et al. (2021). The drag-free control design and in-orbit experimental results of "Taiji-1. Int. J. Mod. Phys. A *36*, 2140019. https://doi.org/10.1142/S0217751X21400194.

16. Zhao, Z.L., and Guo, B.Z. (2016). On Convergence of Nonlinear Active Disturbance Rejection Control for SISO Nonlinear Systems. J. Dyn. Control Syst. *22*, 385–412. https://doi.org/10.1007/s10883-015-9304-5.

17. Gao, Z.Q. (2015). Active disturbance rejection control: From an enduring idea to an emerging technology. Proceedings of the 10th International Workshop on Robot Motion and Control (Poznan), pp. 269–282. https://doi.org/10.1109/RoMoCo.2015.7219747.

18. Chen, W.H., Yang, J., Guo, L., and Li, S. (2016). Disturbance-Observer-Based Control and Related Methods—An Overview. IEEE Trans. Ind. Electron. *63*, 1083–1095. https://doi.org/10.1109/TIE.2015.2478397.

19. Madoński, R., and HERMAN, P. (2015). Survey on methods of increasing the efficiency of extended state disturbance observers. ISA Trans. *56*, 18–27. https://doi.org/10.1016/j.isatra.2014.11.008.

20. Qi, X., Li, J., Xia, Y., and Gao, Z. (2017). On the robust stability of active disturbance rejection control for SISO systems. Circ. Syst. Signal Process. *36*, 65–81. https://doi.org/10.1007/s00034-016-0302-y.

21. Xue, W., and Huang, Y. (2018). Performance analysis of 2-DOF tracking control for a class of nonlinear uncertain systems with discontinuous disturbances. Int. J. Robust Nonlinear Control *28*, 1456–1473. https://doi.org/10.1002/rnc.3972.

22. Long, Y., Du, Z., Cong, L., Wang, W., Zhang, Z., and Dong, W. (2017). Active disturbance rejection control based human

gait tracking for lower extremity rehabilitation exoskeleton. ISA Trans. *67*, 389–397. https://doi.org/10.1016/j.isatra.2017.01.006.

23. Yang, W.Q., Xu, Z., Tang, S., and Zhang, Y.Y. (2016). Self-anti-disturbance based active load shedding control technology for launch vehicles. J. Beijing Univ. Aeronaut. Astronaut. *42*, 130–138. https://doi.org/10.13700/j.bh.1001-5965.2015.0051.

24. Zhu, Y., Zhang, Y., Ma, J., Dong, W., Zhong, X., Pan, Z., and Yao, H. (2019). An enhanced anti-disturbance attitude control law for flexible spacecrafts subject to multiple disturbances. Front. Microbiol. *10*, 274–283. https://doi.org/10.1016/j.conengprac.2018.11.001.

25. Wang, Z., Gong, Z., Chen, Y., Sun, M., and Xu, J. (2020). Practical control implementation of tri-tiltRotor flying wing unmanned aerial vehicles based upon active disturbance rejection control[J]. Proceedings of the Institution of Mechanical Engineers, Part G. J. Aero. Eng. *234*, 943–960. https://doi.org/10.1177/0954410019886963.

26. Yang, H., Geng, X., Zhao, S., and Shi, H. (2020). Dual closed-loop tracking control for wheeled mobile robots via active disturbance rejection control and model predictive control. Plant Physiol. Biochem. *150*, 80–89. https://doi.org/10.1002/rnc.4750.

27. Chen, Z.Q., Sun, M.W., and Yang, R.G. (2014). On the Stability of Linear Active Disturbance Rejection Control. Acta Autom. Sin. *39*, 574–580. https://doi.org/10.3724/SP.J.1004.2013.00574.

28. Xue, W., and Huang, Y. (2015). Performance analysis of active disturbance rejection tracking control for a class of uncertain LTI systems. ISA Trans. *58*, 133–154. https://doi.org/10.1016/j.isatra.2015.05.001.

29. Xue, W., and Huang, Y. (2014). On performance analysis of ADRC for a class of MIMO lower-triangular nonlinear uncertain systems. ISA Trans. *53*, 955–962. https://doi.org/10.1016/j.isatra.2014.02.002.

STAR★METHODS

KEY RESOURCES TABLE

REAGENT or RESOURCE	SOURCE	IDENTIFIER
Software and algorithms		
MATLAB 2021b	MathWorks	https://www.mathworks.com
Microsoft Visio 2021	Microsoft	https://www.microsoft.com/zh-cn/microsoft-365/visio/flowchart-software
Other		
Portable Oscilloscope DL350	YOKOGAWA	https://tmi.yokogawa.com/cn/solutions/products/data-acquisition-equipment/high-speed-data-acquisition/dl350-scopecorder/

RESOURCE AVAILABILITY

Lead contact

Further information and requests for resources and reagents should be directed to and will be fulfilled by the lead contact Aiping Pang (appang@gzu.edu.cn).

Material availability

This study did not generate new unique reagents.

Data and code availability

- All data reported in this paper will be shared by the lead contact upon reasonable request.
- This paper does not report original code.
- Any additional information required to reanalyze the data reported in this paper is available from the lead contact upon request.

EXPERIMENTAL MODEL AND SUBJECT DETAILS

Drag-free satellite motion modeling

To facilitate the description of the dynamical equations for the drag-free satellite and the test mass block, it is necessary to introduce a coordinate system as shown in below figure and to standardize the notation:

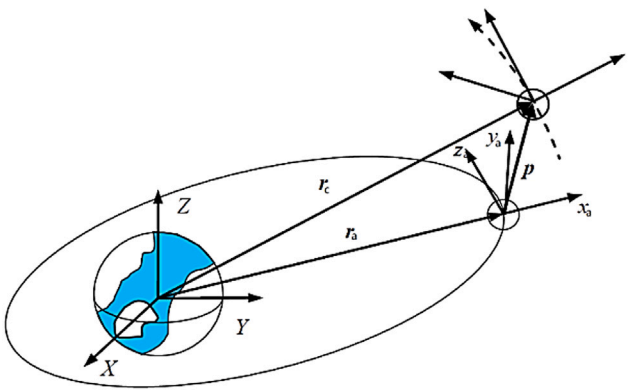

Coordinate system definition

The geocentric equatorial inertial coordinate system (O − XYZ): the origin O is the center of the earth, the X-axis points from the center of the earth to the vernal point of the earth's rotation, the Z-axis points perpendicular to the equatorial plane to the earth's north pole, and the Y-axis and the remaining two axes form a right-handed coordinate system. Satellite orbital coordinate system (relative motion coordinate system) $O_s - X_sY_sZ_s$: the origin is the satellite center of mass, Xa-axis and satellite inertial coordinate system position vector direction opposite; Ya-axis in the satellite orbital plane and Xa-axis perpendicular, along the direction of motion for the positive direction; Za-axis perpendicular to the orbital plane, and the remaining two axes form a right-handed coordinate system.

The schematic diagram of the relative motion of the drag-free satellite and the reference coordinate are shown in below figure. Noting r_a, r_c as the absolute position vector of the test mass and the satellite, the orbital dynamics equations for the satellite and the test mass in the inertial coordinate system Σ_I are given by the follows.

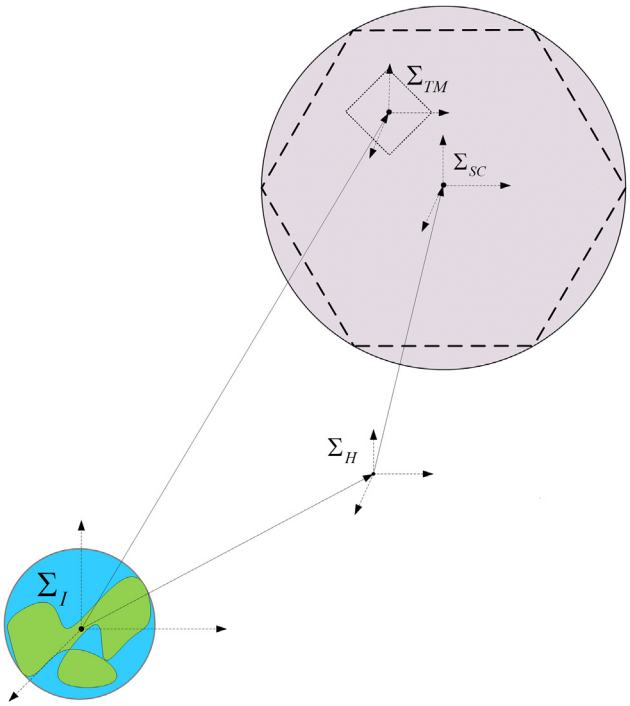

Illustration of the motion and coordinate system of a drag-free satellite

$$\ddot{r}_a = -\frac{\mu r_a}{r_a^3} + f_a \qquad \text{(Equation 1)}$$

$$\ddot{r}_c = -\frac{\mu r_c}{r_c^3} + f_c + \frac{F_c}{m_c} \qquad \text{(Equation 2)}$$

where μ is the gravitational constant; f_a, f_c are the disturbance accelerations acting on the detection mass and the satellite body respectively; F_c is the control force acting on the satellite; m_c is the satellite mass.

The relative position vector of the satellite to the test mass is $\boldsymbol{\rho} = \boldsymbol{r}_c - \boldsymbol{r}_a$. Coupling Equation 1 and Equation 2 yields,

$$\ddot{\boldsymbol{\rho}} = \ddot{\boldsymbol{r}}_c - \ddot{\boldsymbol{r}}_a = -\frac{\mu \boldsymbol{r}_c}{{r_c}^3} + \boldsymbol{f}_c + \frac{\boldsymbol{F}_c}{m_c} - \left(-\frac{\mu \boldsymbol{r}_a}{{r_a}^3} + \boldsymbol{f}_a\right) = \frac{\mu}{ra^3}\left[\boldsymbol{r}_a - \frac{ra^3}{{r_c}^3}\boldsymbol{r}_c\right] + \Delta \boldsymbol{f} + \frac{\boldsymbol{F}_c}{m_c} \qquad \text{(Equation 3)}$$

where Δf is the unknown bounded relative uptake acceleration.

Equation 3 is the expression for the relative position dynamics equation in the inertial coordinate Σ_I. Converting it to the test mass orbit coordinate system Σ_{TM} gives the vector form of the non-linear relative position dynamics model as,

$$\ddot{\boldsymbol{\rho}} = -\dot{\boldsymbol{\omega}}_a \times \boldsymbol{\rho} - 2\boldsymbol{\omega}_a \times \dot{\boldsymbol{\rho}} - \boldsymbol{\omega}_a \times (\boldsymbol{\omega}_a \times \boldsymbol{\rho}) + \frac{\mu}{ra^3}\left[\boldsymbol{r}_a - \frac{r_a^3}{r_c^3}\boldsymbol{r}_c\right] + \Delta \boldsymbol{f} + \frac{\boldsymbol{F}_c}{m_c} \quad \text{(Equation 4)}$$

Where $\boldsymbol{\omega a}$ is the orbital angular velocity of the test mass.

The vectors $\boldsymbol{\rho}$, $\boldsymbol{\omega}_a$, $\boldsymbol{r}_a$ have the following specific form in the test mass reference orbit coordinate system Σ_{TM},

$$\boldsymbol{\rho} = \begin{bmatrix} x \\ y \\ z \end{bmatrix}, \dot{\boldsymbol{\rho}} = \begin{bmatrix} \dot{x} \\ \dot{y} \\ \dot{z} \end{bmatrix}, \boldsymbol{\omega}_a = \begin{bmatrix} 0 \\ 0 \\ \dot{\theta} \end{bmatrix}, \dot{\boldsymbol{\omega}}_a = \begin{bmatrix} 0 \\ 0 \\ \ddot{\theta} \end{bmatrix}, \boldsymbol{r}_a = \begin{bmatrix} -r_a \\ 0 \\ 0 \end{bmatrix}, \boldsymbol{r}_c = \begin{bmatrix} r_a + x \\ y \\ z \end{bmatrix}$$

Substituting the above matrix into Equation 4, we get

$$\begin{cases} \ddot{x} = \dot{\theta}^2 x + \ddot{\theta} y + 2\dot{\theta}\dot{y} + \dfrac{\mu}{r_a^2} - \mu\dfrac{r_a + x}{r_c^3} + \Delta f_x + \dfrac{F_x}{m_c} \\ \ddot{y} = -\ddot{\theta} x + \dot{\theta}^2 y - 2\dot{\theta}\dot{x} - \mu\dfrac{y}{r_c^3} + \Delta f_y + \dfrac{F_y}{m_c} \\ \ddot{z} = -\mu\dfrac{z}{r_c^3} + \Delta f_z + \dfrac{F_z}{m_c} \end{cases} \quad \text{(Equation 5)}$$

Considering the relative displacement of the satellite in orbit from the test mass is much smaller than its orbital radius ($|\boldsymbol{\rho}| \leq |\boldsymbol{r}_c|$), Equation 5 can be linearized and its first order linear expression is shown in the following equation,

$$\begin{cases} \ddot{x} = \dot{\theta}^2 x + \ddot{\theta} y + 2\dot{\theta}\dot{y} + 2\mu\dfrac{x}{r_a^3} + \Delta f_x + \dfrac{F_x}{m_c} \\ \ddot{y} = -\ddot{\theta} x + \dot{\theta}^2 y - 2\dot{\theta}\dot{x} - \mu\dfrac{y}{r_a^3} + \Delta f_y + \dfrac{F_y}{m_c} \\ \ddot{z} = -\mu\dfrac{z}{r_a^3} + \Delta f_z + \dfrac{F_z}{m_c} \end{cases} \quad \text{(Equation 6)}$$

Assuming that the orbit of the satellite is a near circular orbit, then Substituting $\dot{\theta} = n = \sqrt{\frac{\mu}{r_a^3}}$, $\ddot{\theta} = 0$ into the first-order approximate expression Equation 6 yields,

$$\begin{cases} \ddot{x} = 3n^2 x + 2n\dot{y} + \Delta f_x + \dfrac{F_x}{m_c} \\ \ddot{y} = -2n\dot{x} + \Delta f_x + \dfrac{F_y}{m_c} \\ \ddot{z} = -n^2 z + \Delta f_z + \dfrac{F_z}{m_c} \end{cases} \quad \text{(Equation 7)}$$

The interstellar distance of the gravitational wave detection satellite is required to reach about 170,000 km, so the orbital altitude of the drag-free satellite is generally 100,000 km, when $n \rightarrow 0$. Defining the relative displacement $\boldsymbol{\rho} = [x \quad y \quad z]$ as the system output and $\boldsymbol{F_c} = [F_x \quad F_y \quad F_z]$ as the control input, the drag-free control model in the displacement mode can be obtained as follows,

$$G_{DF}(\boldsymbol{s}) = \frac{\boldsymbol{\rho}}{\boldsymbol{F_c}} = \begin{bmatrix} \dfrac{1}{m_c s^2 - k_x} & & \\ & \dfrac{1}{m_c s^2 - k_y} & \\ & & \dfrac{1}{m_c s^2 - k_z} \end{bmatrix} \quad \text{(Equation 8)}$$

Where $\boldsymbol{k} = [k_x \quad k_y \quad k_z]$ is the coupling stiffness and is related to the interaction force $\Delta \boldsymbol{f} \cdot m_c$ between the satellite and the test mass. If the coupling stiffness coefficient between the test mass and the satellite is

neglected and only considering the relative displacement in the direction of the sensitive axis, Equation 8 can be further simplified as,

$$G_{DFx}(s) = \frac{x}{F_x} = \frac{1}{m_c s^2} \quad \text{(Equation 9)}$$

System performance analysis and requirements

The relative position of the Active Disturbance Rejection satellite is modeled as a typical second-order integral link crossing the 0dB line with a slope of −40dB/dec, when the phase angle margin of the system is 0° and the amplitude margin is 0dB. At this point the system has a phase margin of 0° and an amplitude margin of 0dB, which shows that the system is in a critically stable state and that the closed-loop system is susceptible to instability when affected by small disturbances. The special characteristics of the gravitational wave detection mission place the following requirements on the drag-free control system.

(1) Ultra-high precision

The space gravitational wave detection mission, where the signal to be detected is extremely weak and its extremely susceptible to the complex space environment, belongs to the category of high precision measurement experiments. This places extremely stringent requirements on the accuracy of the signal measurement and the stability of the experimental environment: the residual acceleration of the test mass TM along the sensitive axis must be less than 10^{-15} m/sm/s^2/Hz$^{1/2}$, and the satellite displacement control accuracy must reach 4 nm/Hznm/Hz$^{1/2}$.

(2) Ultra-low bandwidth

Depending on the inherent properties and characteristics of the control system, the larger the bandwidth the better the system performance. However, as the sensitive frequency band of gravitational wave detection overlaps with the noise band generated by the actuators (i.e. Micro-Newtonian thrusters) and there is also the effect of measurement noise, the bandwidth of the drag-free control system needs to be controlled to 0.1Hz in order to avoid interference with signals in the sensitive frequency band during detection.

(3) Disturbance suppression

Due to the special nature of the space gravitational wave detection mission of the Lyra satellite, a certain angle needs to be maintained between the detection satellites during the measurement phase (the satellites are steadily pointing towards the distant reference source) and the periodic variations in the angle between the solar vector and the satellite surface (46°–85°) can lead to a large amplitude of the solar pressure on the drag-free satellite. Also owing to the complexity of the external environment in space and the various uncertain sources of interference can have an impact on the Active Disturbance Rejection control. Therefore, in order to cope with the large range of solar pressure variations and the uncertainty of external interference sources during the satellite measurement phase, it is necessary to have a good robustness of the drag-free control system.

(4) Control constraints of the actuator

Most of the thrust actuators currently applied to high-precision drag-free control are electro-propulsion. The electric propulsion has a wide range of adjustable, fast response characteristics, will play an advantage in the future high-precision space missions, but its work also has insufficient ionization, particle motion instability, aging of components and thermal stability fluctuations caused by long working hours, the storage and supply system of flow changes and other problems. The electric thruster is regulated by a variety of parameters such as mass flow and voltage, and there is a certain inertial lag in the mass supply system, which makes the actuator unable to respond quickly to a wide range of thrust changes (i.e. there are certain constraints on the control input to achieve a wide range of thrust jumps). Compared to the external disturbances of the complex space environment, the internal disturbances and noise generated by the micro-thruster are "low frequency disturbances" that seriously affect the performance of the system. Therefore, we must take into account the output constraints and noise characteristics of the actuators to design drag-free control and ensure that the designed controller is feasible for practical applications.

METHOD DETAILS

Control system design based on ADRC

Facing many problems such as the difficulty of accurately modeling various interference sources in complex space environments, the existence of output constraints and internal noise in the propulsion system, the influence of inherent measurement noise, and the ultra-low bandwidth requirements of the control system, the ADRC technology has unique advantages: 1) It does not rely on the exact model of the controlled object, based on the idea of total perturbation to transform the control object into an integral standard type, which is obviously suitable for the gravitational wave detection which has multiple sources of interference that cannot be accurately modeled and analyzed and has a non-linear control problem. 2) The tracking differentiator has the effect of smooth filtering, which can solve the overshooting problem caused by the enlarged measurement noise from the differentiator and the constrained thrust output. 3) The feedback controller can be embedded with different control methods such as robust controllers or non-linear controllers depending on the specific system requirements. Thus, a feedback control method can be designed to achieve high accuracy while ensuring ultra-low bandwidth for gravitational wave detection. Moreover, the theoretical framework of the ADRC is mature and has certain feasibility and realizability.

Figure below shows a scheme for a drag-free control system based on ADRC approach. An extended state observer first estimates the disturbance to the system and compensates it feedforward, while the output of the system containing the measurement noise is filtered and estimated as a feedback controller input. The feedback controller acts as a drag-free controller to achieve high performance and bandwidth-limited requirements of the system while ensuring robustness.

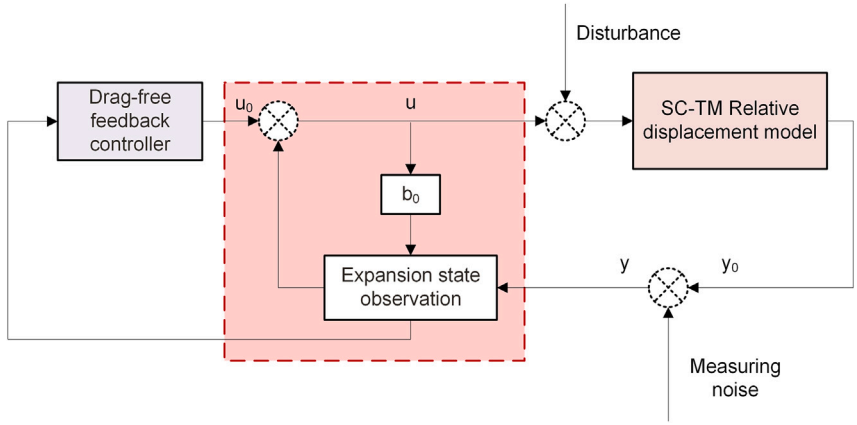

Block diagram of a drag-free control system based on ADRC

Considering the object properties of a drag-free control system as a pure second-order integral, we use a second-order expanded state observer in LADRC to estimate the output state and the total disturbance of the system. A linearly extended state observer (LESO) is built as shown below,

$$\begin{cases} e = z_1 - y \\ \dot{z}_1 = z_2 - \beta_1 e \\ \dot{z}_2 = z_3 - \beta_2 e + b u_0 \\ \dot{z}_3 = -\beta_3 e \end{cases} \quad \text{(Equation 10)}$$

The $\boldsymbol{\beta} = [\beta_1 \quad \beta_2 \quad \beta_3]$ is the gain of the observer. By selecting the appropriate observer gain, the observed value z can be made to converge to the true state value of the system. We use the observer gain tuning method in Linear Active Disturbance Rejection Control (LADRC), where the observer gain is obtained by adjusting the observer bandwidth. Since the system under control is a second-order system, the observer gain is determined by the following equation,

$$\begin{cases} \beta_1 = 3\omega_o \\ \beta_1 = 3\omega_o^2 \\ \beta_1 = \omega_o^3 \end{cases} \quad \text{(Equation 11)}$$

As shown in below figure external disturbances for different observer bandwidths are shown. It can be seen that the response of the observer is faster as the bandwidth increases, but the observation bandwidth is too large to amplify the measurement noise of the system, which reduces the signal-to-noise ratio in the observations and affects the feedforward compensation for the system. Considering the speed and accuracy of the observed response to system disturbances, the observation bandwidth of the second-order LESO is set to $\omega_o = 2.5rad/s$, and the corresponding gain of the dilated state observer is $\boldsymbol{\beta} = [7.5 \quad 18.75 \quad 15.625]$.

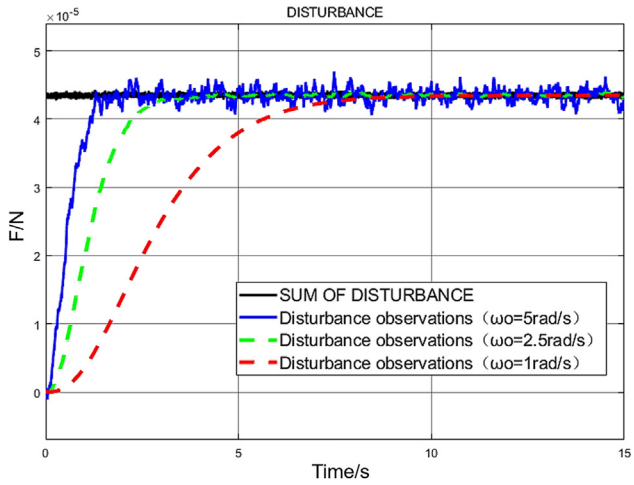

Effect of the observer with different observation bandwidths

Based on the analysis, the drag-free control system needs to satisfy both the high precision index and the robust performance. For the robustness-constrained control problem with high precision performance requirements, we usually consist of two strategies: one is to first design a controller that satisfies the high precision performance requirements of the system, then verify its robustness, and then iteratively optimize the controller; the other is to solve the system under the premise of satisfying the robustness constraints of the system to satisfy the high precision performance of the system under the premise of satisfying the robustness constraints of the system. In this paper, based on the self-turbulence control technology, H_∞ feedback control is selected as the controller based on the self-turbulence control method to solve the integrated controller that satisfies the high precision and low bandwidth performance requirements of the system under the premise of ensuring the high robustness of the drag-free control system.

(1) Standard PS/T issues

Since both system performance and robustness need to be considered, we organize the drag-free control problem as a standard H_∞ control problem. In Standard PS/T issues, "PS" is plant sensitivity, "T" is transfer. The logic block diagram is represented in below figure, where G is the generalized controlled object, z is the performance-weighted output, y is the system output, u is the control input, and w is the external disturbance input to the system.

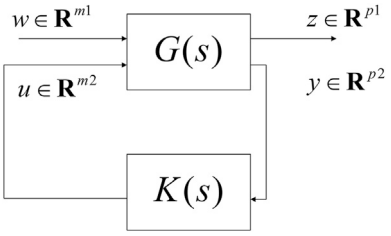

Block diagram of standard H_∞ problem

The external input of the drag-free control system contains non-conservative force perturbations such as solar pressure and measurement noise, and the controlled object contains a double integration link. In order to avoid the phenomenon that the zero point of the controller and the poles of the controlled object are

eliminated relative to each other in the S/T problem, which causes the uncontrollability of the system, we adopt the PS/T problem for the controller design.

Figure below shows the block diagram of the standard PS/T problem.

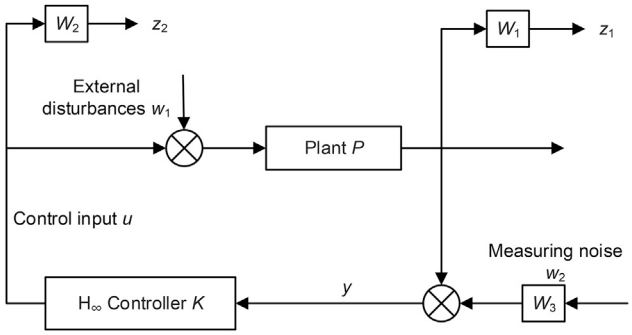

PS/T problem block diagram

The broad object is $G = \begin{bmatrix} W_1P & 0 & W_1P \\ 0 & 0 & W_2 \\ P & W_3 & P \end{bmatrix}$. The corresponding optimization problem is

$$\min \left\| \begin{matrix} W_1PS \\ W_2T \\ W_3R \end{matrix} \right\|_\infty = \gamma \qquad \text{(Equation 12)}$$

Equation 12 shows that the object P appears in the performance index in a separate form, unlike the S/T problem where it appears as a product of PKs, so the zero point in the controller does not create a pair-cancellation problem with the poles of the object P.

(2) Performance weighting function design

According to the above analysis, there are three requirements for the design of drag-free control system: ultra-high accuracy, ultra-low bandwidth and disturbance suppression requirements. H∞ control is to get the optimal solution of (Equation 9) under the premise of ensuring the robustness requirements, so the problem solution based on (Equation 9) is mainly to optimize the output accuracy and low bandwidth as the target, and solve the H_∞ controller to meet the performance requirements by selecting the appropriate performance weighting function. Where PS is the closed-loop transfer function from the disturbance input W_1 to the object P output, representing the disturbance decay characteristics of the system, so it W_1PS also represents the performance index of the system itself, indicating the suppression characteristics of the external disturbance is also the output accuracy of the system, that is, the performance weighting function set the controller is required to have an integral law, so W_1(s) should be equipped with an integral link, in order to make the integral link in the control law does not affect the stability, hoping that it is in After 10 rad/s decay, take the performance power function

$$W_1(s) = \frac{\rho(0.1s+1)}{(s+\varepsilon)^2} \qquad \text{(Equation 13)}$$

where ρ is the parameter to be optimized and ε is the additional parameter to avoid the appearance of imaginary axis poles, which is generally taken as 0.001. The second term W_2(s) in Equation 12 is a limitation on the system bandwidth considering the gravitational wave sensitive band in the system, the bandwidth of the drag-free control system requires less than 1 rad/s, but because the controlled object P is second order, so the slope after the 0dB line is required to take +40dB/dec, and at the same time consider the power function are true rational functions, so it is taken W2(s) as

$$W_2(s) = \frac{s^2}{(0.001s+1)^2} \qquad \text{(Equation 14)}$$

(3) Feedback controller performance analysis

According to the above selection of the weighting function, the H_∞ problem can be solved to obtain the optimization parameter $\rho = 50$ when $\gamma = 2.50$, the corresponding H_∞ controller is

$$K_\infty(s) = \frac{-25.417(s+1000)^2(s+0.3858)(s^2+0.3838s+0.1882)}{(s+99.26)(s+2.4)(s+0.05192)(s+0.04801)(s^2+28.07s+396.8)} \quad \text{(Equation 15)}$$

By omitting the higher order terms with poles above 103 and also removing the additional perturbation parameter terms in the design process, the reduced order controller is obtained as,

$$K(s) = \frac{-2.5417 \times 10^7(s^2+0.3838s+0.1882)}{s(s+99.26)(s+2.4)(s^2+28.07s+396.8)} \quad \text{(Equation 16)}$$

By verifying the infinite parity of each component in (Equation 9), the Sigma values of each component are smaller than the final optimization index of H_∞, as shown in below figure, GAM is γ, L is the transfer function of the forward channel.

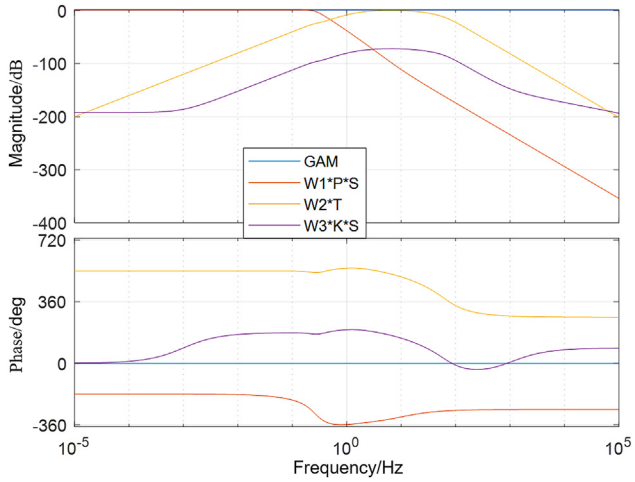

Paradigm index validation

According to the designed controller, the open-loop frequency characteristics of the drag-free control system after adding the H_∞ controller are shown in below figure, and the phase angle margin of the system is changed from 0 to 180, and the bandwidth of the system is 0.1Hz, which meets the performance requirements of the bandwidth of the drag-free control system in the gravitational wave detection mission.

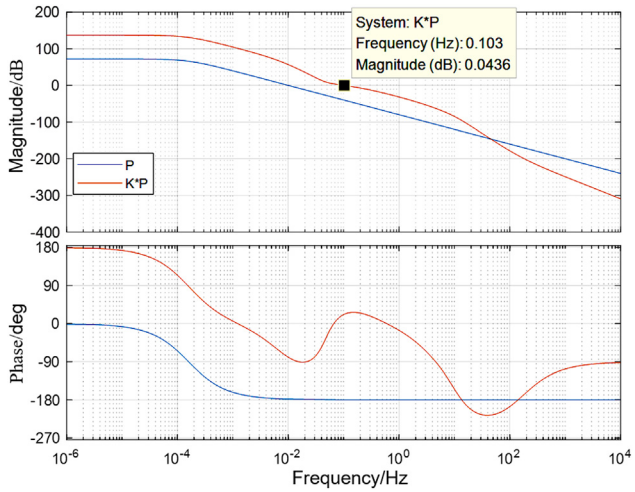

Open-loop frequency characteristics of the system based on H_∞ control

Figures below show the Bode plots of the singular values of the sensitivity function S and the closed-loop transfer function T, respectively, and the corresponding weight functions, which W_1 determine the performance in the low frequency band; and W_2 this item reflects the robustness of the system. The robustness of the controller for object uptake in the middle frequency band is relatively weak compared to the low and high frequency bands, which is required to achieve the ultra-high accuracy performance of the system.

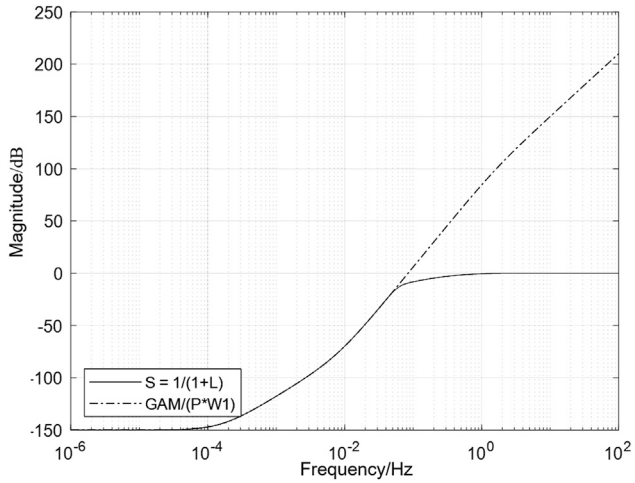

Singular values of the sensitivity function S

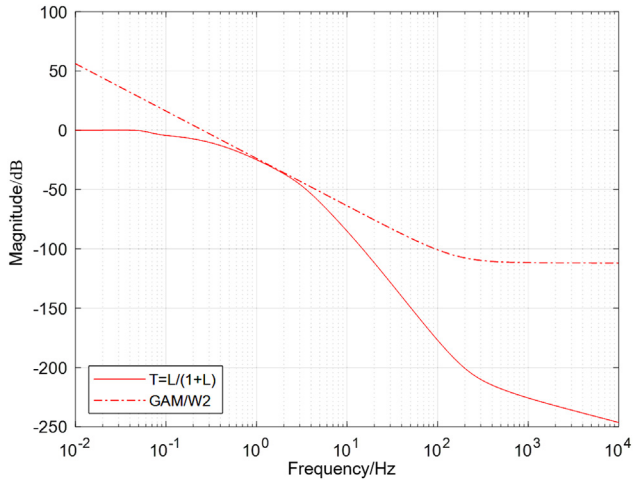

Singular values of the closed-loop transfer function T

Figure below shows the singular value plot of the controller sensitivity function KS and the corresponding power function, which shows that the controller has differential characteristics in the low frequency band, while the controller gain is limited to some extent in the high frequency band.

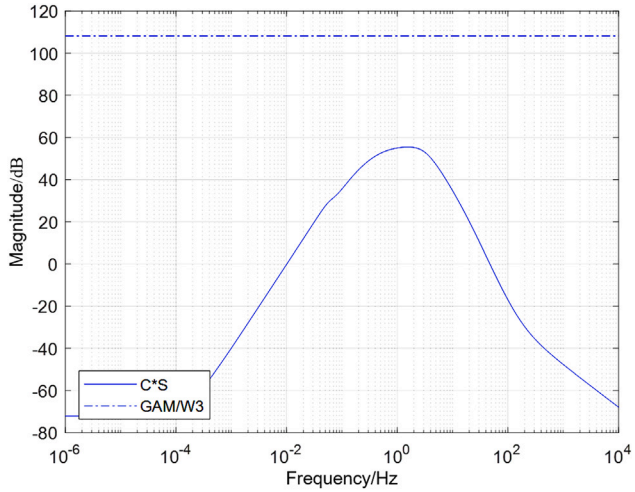

Singular values of the feedback controller KS

QUANTIFICATION AND STATISTICAL ANALYSIS

Microsoft Visio 2021 is used to generate the visual images in the manuscript. The thrust noise signals are captured by the DL350 digital oscilloscope. MATLAB 2021b is used to process experimental data and generate visual images in the manuscript. The power spectrum curves of relative displacement and residual acceleration are obtained separately by MATLAB 2021b to analyze the output characteristics of the system.